Published for SISSA by Springer

Received: January 27, 2016
Revised: March 24, 2016
Accepted: April 16, 2016
Published: May 3, 2016

Precision measurement of the $\eta \to \pi^+\pi^-\pi^0$ Dalitz plot distribution with the KLOE detector

The KLOE-2 collaboration

A. Anastasi,[a,b] D. Babusci,[b] G. Bencivenni,[b] M. Berlowski,[c] C. Bloise,[b] F. Bossi,[b] P. Branchini,[d] A. Budano,[e,d] L. Caldeira Balkeståhl,[f] B. Cao,[f] F. Ceradini,[e,d] P. Ciambrone,[b] F. Curciarello,[a,g,h] E. Czerwiński,[i] G. D'Agostini,[j,k] E. Danè,[b] V. De Leo,[d] E. De Lucia,[b] A. De Santis,[b] P. De Simone,[b] A. Di Cicco,[e,d] A. Di Domenico,[j,k] R. Di Salvo,[l] D. Domenici,[b] A. D'Uffizi,[b] A. Fantini,[m,l] G. Felici,[b] S. Fiore,[n,k] A. Gajos,[i] P. Gauzzi,[j,k] G. Giardina,[a,g] S. Giovannella,[b] E. Graziani,[d] F. Happacher,[b] L. Heijkenskjöld,[f] W. Ikegami Andersson,[f] T. Johansson,[f] D. Kamińska,[i] W. Krzemien,[c] A. Kupsc,[f] S. Loffredo,[e,d] G. Mandaglio,[o,p] M. Martini,[b,q] M. Mascolo,[b] R. Messi,[m,l] S. Miscetti,[b] G. Morello,[b] D. Moricciani,[l] P. Moskal,[i] M. Papenbrock,[f] A. Passeri,[d] V. Patera,[r,k] E. Perez del Rio,[b] A. Ranieri,[s] P. Santangelo,[b] I. Sarra,[b] M. Schioppa,[t,u] M. Silarski,[b] F. Sirghi,[b] L. Tortora,[d] G. Venanzoni,[b] W. Wiślicki[c] and M. Wolke[f]

[a] *Dipartimento di Fisica e Scienze della Terra dell'Università di Messina, Messina, Italy*
[b] *Laboratori Nazionali di Frascati dell'INFN, Frascati, Italy*
[c] *National Centre for Nuclear Research, Warsaw, Poland*
[d] *INFN Sezione di Roma Tre, Roma, Italy*
[e] *Dipartimento di Matematica e Fisica dell'Università "Roma Tre", Roma, Italy*
[f] *Department of Physics and Astronomy, Uppsala University, Uppsala, Sweden*
[g] *INFN Sezione di Catania, Catania, Italy*
[h] *Novosibirsk State University, 630090 Novosibirsk, Russia*
[i] *Institute of Physics, Jagiellonian University, Cracow, Poland*
[j] *Dipartimento di Fisica dell'Università "Sapienza", Roma, Italy*
[k] *INFN Sezione di Roma, Roma, Italy*
[l] *INFN Sezione di Roma Tor Vergata, Roma, Italy*
[m] *Dipartimento di Fisica dell'Università "Tor Vergata", Roma, Italy*
[n] *ENEA UTTMAT-IRR, Casaccia R.C., Roma, Italy*
[o] *Dipartimento di Scienze Chimiche, Biologiche, Farmaceutiche ed Ambientali dell'Università di Messina, Messina, Italy*
[p] *INFN Gruppo collegato di Messina, Messina, Italy*
[q] *Dipartimento di Scienze e Tecnologie applicate, Università "Guglielmo Marconi", Roma, Italy*

doi:10.1007/JHEP05(2016)019

JHEP05(2016)019

[r] *Dipartimento di Scienze di Base ed Applicate per l'Ingegneria dell'Università "Sapienza", Roma, Italy*
[s] *INFN Sezione di Bari, Bari, Italy*
[t] *Dipartimento di Fisica dell'Università della Calabria, Rende, Italy*
[u] *INFN Gruppo collegato di Cosenza, Rende, Italy*

E-mail: Andrzej.Kupsc@physics.uu.se

Abstract: Using $1.6\,\mathrm{fb}^{-1}$ of $e^+e^- \to \phi \to \eta\gamma$ data collected with the KLOE detector at DAΦNE, the Dalitz plot distribution for the $\eta \to \pi^+\pi^-\pi^0$ decay is studied with the world's largest sample of $\sim 4.7 \cdot 10^6$ events. The Dalitz plot density is parametrized as a polynomial expansion up to cubic terms in the normalized dimensionless variables X and Y. The experiment is sensitive to all charge conjugation conserving terms of the expansion, including a gX^2Y term. The statistical uncertainty of all parameters is improved by a factor two with respect to earlier measurements.

Keywords: e+-e- Experiments, QCD

ArXiv ePrint: 1601.06985

JHEP05(2016)019

Contents

JHEP05(2016)019

1 Introduction

The isospin violating $\eta \to \pi^+\pi^-\pi^0$ decay can proceed via electromagnetic interactions or via strong interactions due to the difference between the masses of u and d quarks. The electromagnetic part of the decay amplitude is long known to be strongly suppressed [1, 2]. The recent calculations performed at next-to-leading order (NLO) of the chiral perturbation theory (ChPT) [3, 4] reaffirm that the decay amplitude is dominated by the isospin violating part of the strong interaction.

Defining the quark mass ratio, Q, as

$$Q^2 \equiv \frac{m_s^2 - \hat{m}^2}{m_d^2 - m_u^2} \qquad \text{with } \hat{m} = \frac{1}{2}(m_d + m_u), \tag{1.1}$$

the decay amplitude at up to NLO ChPT is proportional to Q^{-2} [5]. The definition in eq. (1.1), neglecting $\hat{m}^2/m_s^2$, gives an ellipse in the $m_s/m_d, m_u/m_d$ plane with major semi-axis Q [6]: a determination of Q puts a stringent constraint on the light quark masses. The proportionality factor could be determined from ChPT calculations in the isospin limit.

Using Dashen's theorem [7] to account for the electromagnetic effects, Q can be determined at the lowest order from a combination of kaon and pion masses. With this value of $Q = 24.2$, the ChPT results for the $\eta \to \pi^+\pi^-\pi^0$ decay width at LO, $\Gamma_{LO} = 66\,\text{eV}$, and NLO, $\Gamma_{NLO} = 160 - 210\,\text{eV}$ [8]. The calculations should be compared to the present experimental value of $\Gamma_{exp} = 300 \pm 11\,\text{eV}$ [9]. The experiment-theory discrepancy could originate from higher order contributions to the decay amplitude or from corrections to the Q value.

To understand the role of the higher order contributions a full NNLO ChPT calculation was carried out and it gives $\Gamma_{NNLO} = 230 - 270\,\text{eV}$ within the Dashen limit [10]. The

NNLO result depends on the values of a large number of the coupling constants of the chiral lagrangian which are not known precisely. On the other hand it is known that the $\pi\pi$ rescattering plays an important role in the decay, giving about half of the correction from the LO to the NLO result [8]. The rescattering can be accounted for to all orders using dispersive integrals and precisely known $\pi\pi$ phase shifts. In the dispersive calculations two approaches are possible. The first is to improve ChPT predictions starting from the NLO ChPT calculations. In the second approach one can determine the proportionality factor for the Q^{-2} in the $\eta \to \pi^+\pi^-\pi^0$ decay amplitude from fits to the experimental Dalitz plot data and by matching the results to the LO amplitude in the region where it could be considered accurate. Both approaches are pursued by three theory groups: refs. [13–15]. In the first approach the reliability of the calculations could be verified by a comparison with the experimental Dalitz plot data. Conversely, in the second approach precise experimental Dalitz plot distributions could be used to determine the quark ratio Q without relying on the higher order ChPT calculations.

Two other recent theoretical descriptions of the $\eta \to 3\pi$ decay amplitude include unitarized ChPT (UChPT) [11] and non-relativistic effective field theory (NRFT) [12]. UChPT is a model dependent approach which uses relativistic coupled channels and allows for simultaneous treatment of all hadronic η and η' decays. The NRFT framework is used to study higher order isospin breaking effects in the final state interactions.

For the $\eta \to \pi^+\pi^-\pi^0$ Dalitz plot distribution, the normalized variables X and Y are commonly used:

$$X = \sqrt{3}\frac{T_{\pi^+} - T_{\pi^-}}{Q_\eta} \tag{1.2}$$

$$Y = \frac{3T_{\pi^0}}{Q_\eta} - 1 \tag{1.3}$$

with

$$Q_\eta = T_{\pi^+} + T_{\pi^-} + T_{\pi^0} = m_\eta - 2m_{\pi^+} - m_{\pi^0}. \tag{1.4}$$

T_i are kinetic energies of the pions in the η rest frame. The squared amplitude of the decay is parametrized by a polynomial expansion around $(X, Y) = (0, 0)$:

$$|A(X,Y)|^2 \simeq N(1 + aY + bY^2 + cX + dX^2 + eXY + fY^3 + gX^2Y + hXY^2 + lX^3 + \ldots). \tag{1.5}$$

The Dalitz plot distribution can then be fit using this formula to extract the parameters $a, b, \ldots$, usually called the Dalitz plot parameters. Note that coefficients multiplying odd powers of X (c, e, h and l) must be zero assuming charge conjugation invariance.

The experimental values of the Dalitz plot parameters are shown in table 1 together with the parametrization of theoretical calculations. The last three most precise measurements include the 2008 analysis from KLOE which was based on $1.34 \cdot 10^6$ events [19]. There is some disagreement among the experiments, specially for the b but also for the a parameter. Both b and the f parameters from theory deviate from the experimental values. The new high statistics measurement presented in this paper can help to clarify the tension among the experimental results, and can be used as a more precise input for the dispersive calculations.

JHEP05(2016)019

Experiment	$-a$	b	d	f	$-g$
Gormley(70) [16]	1.17 ± 0.02	0.21 ± 0.03	0.06 ± 0.04	–	–
Layter(73) [17]	1.080 ± 0.014	0.03 ± 0.03	0.05 ± 0.03	–	–
CBarrel(98) [18]	1.22 ± 0.07	0.22 ± 0.11	0.06(fixed)	–	–
KLOE(08) [19]	$1.090 \pm 0.005^{+0.019}_{-0.008}$	$0.124 \pm 0.006 \pm 0.010$	$0.057 \pm 0.006^{+0.007}_{-0.016}$	$0.14 \pm 0.01 \pm 0.02$	–
WASA(14) [20]	1.144 ± 0.018	$0.219 \pm 0.019 \pm 0.047$	$0.086 \pm 0.018 \pm 0.015$	0.115 ± 0.037	–
BESIII(15) [21]	$1.128 \pm 0.015 \pm 0.008$	$0.153 \pm 0.017 \pm 0.004$	$0.085 \pm 0.016 \pm 0.009$	$0.173 \pm 0.028 \pm 0.021$	–
Calculations					
ChPT LO [10]	1.039	0.27	0	0	–
ChPT NLO [10]	1.371	0.452	0.053	0.027	–
ChPT NNLO [10]	1.271 ± 0.075	0.394 ± 0.102	0.055 ± 0.057	0.025 ± 0.160	–
dispersive [22]	1.16	0.26	0.10	–	–
simplified disp [5]	1.21	0.33	0.04	–	–
NREFT [12]	1.213 ± 0.014	0.308 ± 0.023	0.050 ± 0.003	0.083 ± 0.019	0.039 ± 0.002
UChPT [11]	1.054 ± 0.025	0.185 ± 0.015	0.079 ± 0.026	0.064 ± 0.012	–

Table 1. Summary of Dalitz plot parameters from experiments and theoretical predictions.

2 The KLOE detector

The KLOE detector at the DAΦNE e^+e^- collider in Frascati consists of a large cylindrical Drift chamber (DC) and an electromagnetic calorimeter (EMC) in a 0.52 T axial magnetic field. The DC [23] is 4 m in diameter and 3.3 m long and is operated with a helium - isobutane gas mixture (90% - 10%). Charged particles are reconstructed with a momentum resolution of $\sigma(p_\perp)/p_\perp \simeq 0.4\%$.

The EMC [24] consists of alternating layers of lead and scintillating fibers covering 98% of the solid angle. The lead-fiber layers are arranged in $\sim (4.4 \times 4.4)$ cm^2 cells, five in depth, and these are read out at both ends. Hits in cells close in time and space are grouped together in clusters. Cluster energy is obtained from the signal amplitude and has a resolution of $\sigma(E)/E = 5.7\%/\sqrt{E(\mathrm{GeV})}$. Cluster time, t_{cluster}, and position are energy weighted averages, with time resolution $\sigma(t) = (57\ \mathrm{ps})/\sqrt{E(\mathrm{GeV})} \oplus 100$ ps. The cluster position along the fibers is obtained from time differences of the signals.

The KLOE trigger [25] uses both EMC and DC information. The trigger conditions are chosen to minimize beam background. In this analysis, events are selected with the calorimeter trigger, requiring two energy deposits with $E > 50$ MeV for the barrel and $E > 150$ MeV for the endcaps. The trigger signal, that is phase locked with the clock coming from DAΦNE radio frequency (2.7 ns), cannot be used as the time scale origin because of the large spread of arrival times of produced particles (photons, kaons, etc.). Thus, the interaction time is obtained event by event from the data exploiting the excellent timing performances of the calorimeter (230 ps for 50 MeV photons). A discrete search of different bunch times is done by constraining the arrival time of promptest clusters with $E > 50$ MeV.

The analysis is performed using data collected at the ϕ meson peak with the KLOE detector in 2004-2005, and corresponds to an integrated luminosity of $\sim 1.6\,\mathrm{fb}^{-1}$. Due to DAΦNE crossing angle ϕ mesons have a small horizontal momentum, $\mathbf{p}_\phi$ of about 13 MeV/c. The η mesons are produced in the radiative decay $\phi \to \eta\gamma_\phi$. The photon from the ϕ radiative decay, γ_ϕ, has an energy $E \sim 363$ MeV. The data sample used for this analysis is independent and about four times larger than the one used in the previous KLOE(08) $\eta \to \pi^+\pi^-\pi^0$ Dalitz plot analysis [19].

The reconstructed data are sorted by an event classification procedure which rejects beam and cosmic ray backgrounds and splits the events into separate streams according to their topology [26]. The beam and background conditions are monitored. The corresponding parameters are stored for each run and included in the GEANT3 based Monte Carlo (MC) simulation of the detector. The event generators for the production and decays of the ϕ-meson include simulation of initial state radiation. The final state radiation is included for the simulation of the signal process. The simulation of $e^+e^- \to \omega\pi^0$ process (an important background in this analysis) assumes a cross section of 8 nb. The simulations of the background channels used in this analysis correspond to the integrated luminosity of the experimental data set, while the signal simulation corresponds to ten times larger luminosity.

JHEP05(2016)019

3 Event selection

Two tracks of opposite curvature and three neutral clusters are expected in the final state of the chain $e^+e^- \to \phi \to \eta\gamma_\phi \to \pi^+\pi^-\pi^0\gamma_\phi \to \pi^+\pi^-\gamma\gamma\gamma_\phi$. Selection steps are listed below:

- A candidate event has at least three prompt neutral clusters in the EMC. The clusters are required to have energy at least 10 MeV and polar angles $23^\circ < \theta < 157^\circ$, where θ is calculated from the distance of the cluster to the beam crossing point ($R_{\rm cluster}$). The time of the prompt clusters should be within the time window for massless particles, $|t_{\rm cluster} - R_{\rm cluster}/c| < 5\sigma(t)$, while neutral clusters do not have an associated track in the DC.

- At least one of the prompt neutral clusters has energy greater than 250 MeV. The highest energy cluster is assumed to originate from the γ_ϕ photon.

- The two tracks within a cylindrical volume with radius 8 cm and axial position ± 15 cm from the beam crossing, and with opposite curvature, are chosen. In the following these tracks are assumed to be due to charged pions. Discrimination against electron contamination from Bhabha scattering is achieved by means of Time Of Flight as discussed in the following.

- P_ϕ, the four-momentum of the ϕ meson, is determined using the beam-beam energy $\sqrt{s}$ and the ϕ transverse momentum measured in Bhabha scattering events for each run.

- The γ_ϕ direction is obtained from the position of the EMC cluster while its energy/momentum is calculated from the two body kinematics of the $\phi \to \eta\gamma_\phi$ decay:

$$E_{\gamma_\phi} = \frac{m_\phi^2 - m_\eta^2}{2 \cdot \left(E_\phi - |\mathbf{p}_\phi| \cos\theta_{\phi,\gamma}\right)}$$

  where $\theta_{\phi,\gamma}$ is the angle between the ϕ and the γ_ϕ momenta. The four-momentum of the η meson is then: $P_\eta = P_\phi - P_{\gamma_\phi}$.

- The π^0 four-momentum is calculated from the missing four-momentum to η and the charged pions: $P_{\pi^0} = P_\eta - P_{\pi^+} - P_{\pi^-}$.

- To reduce the Bhabha scattering background, the following two cuts are applied:

  - a cut in the $(\theta_{+\gamma},\theta_{-\gamma})$ plane as shown in figure 1, where $\theta_{+\gamma}(\theta_{-\gamma})$ is the angle between the $\pi^+(\pi^-)$ and the closest photon from π^0 decay.
  - a cut in the $(\Delta t_e, \Delta t_\pi)$ plane as shown in figure 2, to discriminate electrons from pions, where Δt_e, Δt_π are calculated for tracks which have an associated cluster, $\Delta t_{e/\pi} \equiv t_{{\rm track}_{e/\pi}} - t_{\rm cluster}$, where $t_{{\rm track}_{e/\pi}}$, is the expected arrival time to EMC for e/π with the measured momentum, and $t_{\rm cluster}$ the measured time of the EMC cluster.

JHEP05(2016)019

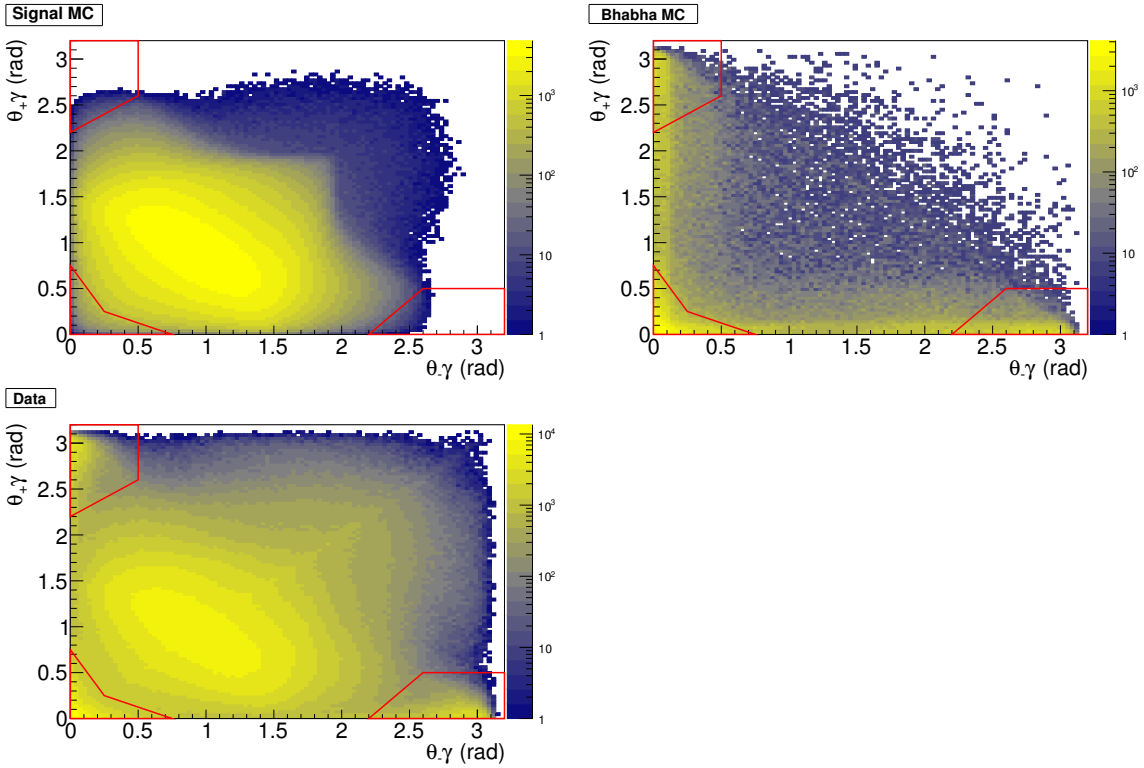

Figure 1. (Color online) $\theta_{+\gamma}$ *vs* $\theta_{+\gamma}$ angle plot. The three panels correspond to signal MC, Bhabha MC and the data. The three regions in the corners with borders marked by red lines represent the Bhabha rejection cut applied in the analysis.

- To improve the agreement between simulation and data, a correction for the relative yields of: (i) $e^+e^- \to \omega\pi^0$, and (ii) sum of all other backgrounds, with respect to the signal is applied. The correction factors are obtained from a fit to the distribution of the azimuthal angle between the π^0 decay photons, in the π^0 rest frame, $\theta^*_{\gamma\gamma}$ (figure 3). The uncertainties of the correction factors are taken as half of the difference between the value obtained from the corresponding fit to the distribution of the missing mass squared, $P^2_{\pi^0}$ (figure 4).

- To further reduce the background contamination, two more cuts are applied:

  – $\theta^*_{\gamma\gamma} > 165°$, see figure 3;

  – $||P_{\pi^0}| - m_{\pi^0}| < 15\,\text{MeV}$, see figure 4;

The overall signal efficiency is 37.6% at the end of the analysis chain and the signal to background ratio is 133.

As can be seen in figures 3, 4 and 6 the agreement of simulation with the experimental data is good.

JHEP05(2016)019

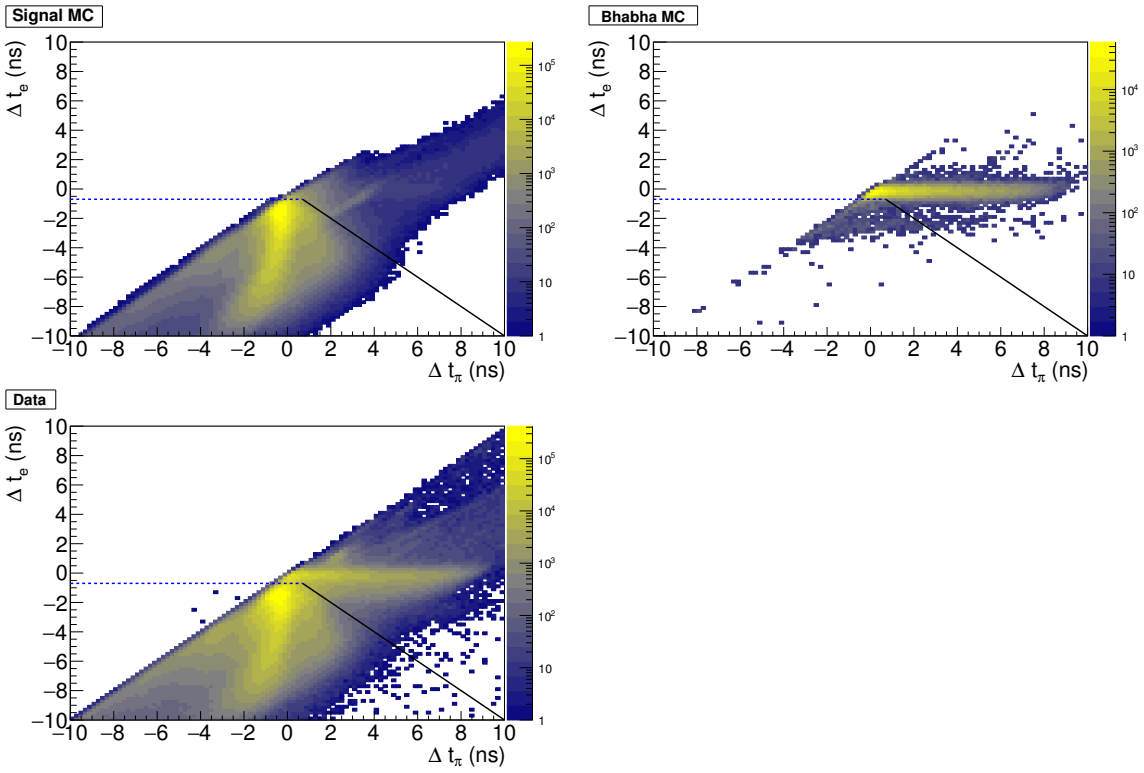

Figure 2. (Color online) Δt_e *vs* Δt_π plots for signal MC, Bhabha MC and the data. Events above the blue (dotted) line or above the black (full) line are rejected.

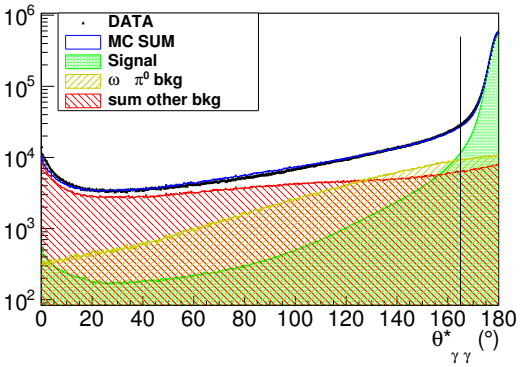

Figure 3. (Color online) Azimuthal angle difference between the π^0 decay photons in the π^0 rest frame, $\theta^*_{\gamma\gamma}$, with the MC contributions scaled. The cut $\theta^*_{\gamma\gamma} > 165°$ is shown by the vertical line.

JHEP05(2016)019

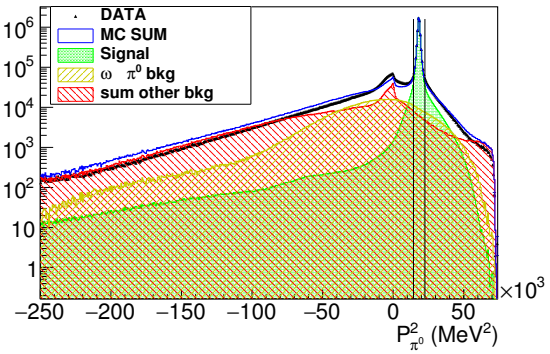

Figure 4. (Color online) Missing mass squared, $P^2_{\pi^0}$, with the MC contributions scaled. The cut $||P_{\pi^0}| - m_{\pi^0}| < 15\,\text{MeV}$ is represented by the two vertical lines.

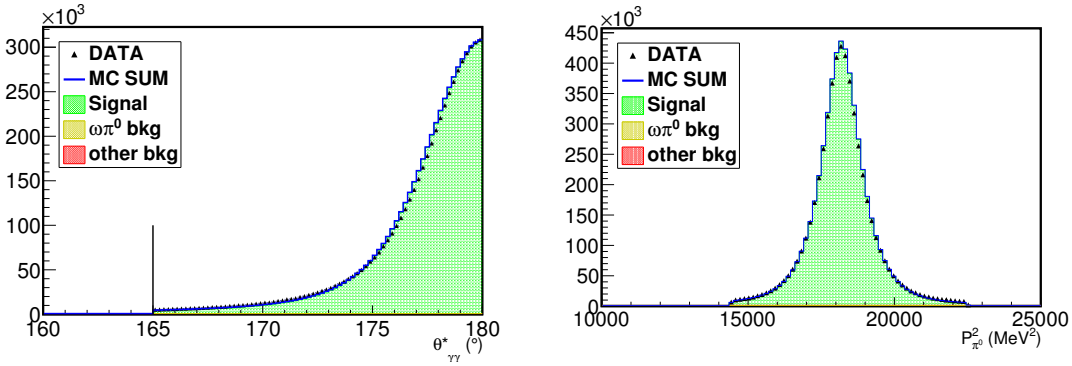

Figure 5. (Color online) The distributions of $\theta^*_{\gamma\gamma}$ (left) and $P^2_{\pi^0}$ (right) after all the analysis cuts.

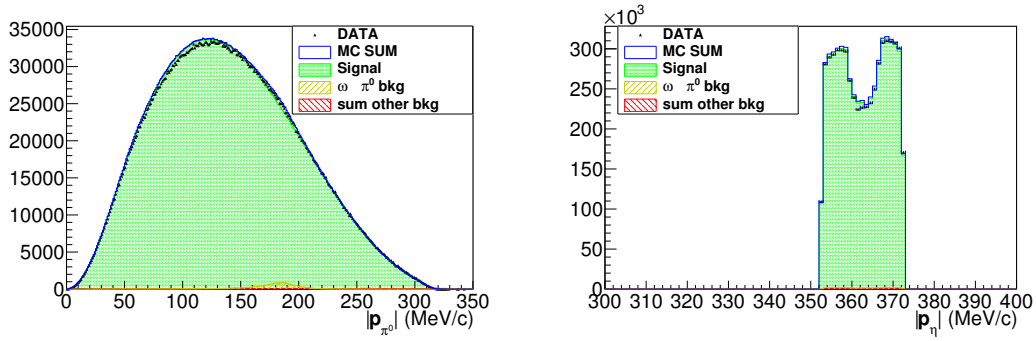

Figure 6. Distribution of the reconstructed momentum of π^0 (left) and η (right) for the data and MC.

JHEP05(2016)019

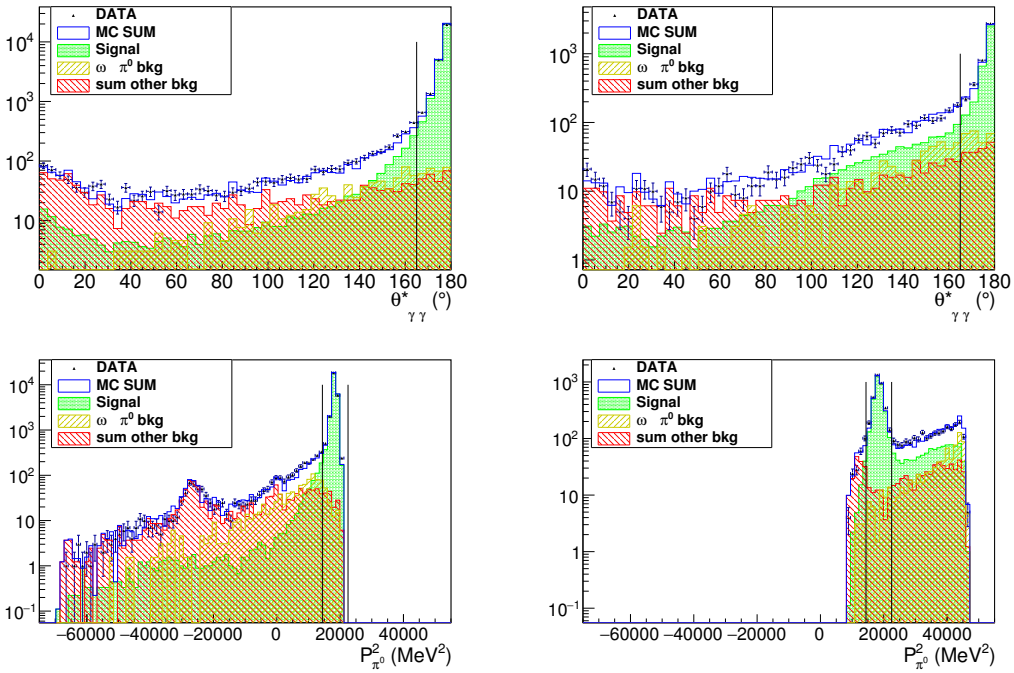

Figure 7. (Color online) Top: $\theta^*_{\gamma\gamma}$ angle distribution with the MC contributions scaled; the selected region is at the right of the vertical line. Bottom: missing mass squared, $P^2_{\pi^0}$, with the MC contributions scaled. The selected region is between the vertical lines. Left/right: bin of the Dalitz plot with the largest/smallest number of entries, corresponding to $(X, Y) = (0.000, -0.850)$ and $(X, Y) = (-0.065, 0.750)$, respectively.

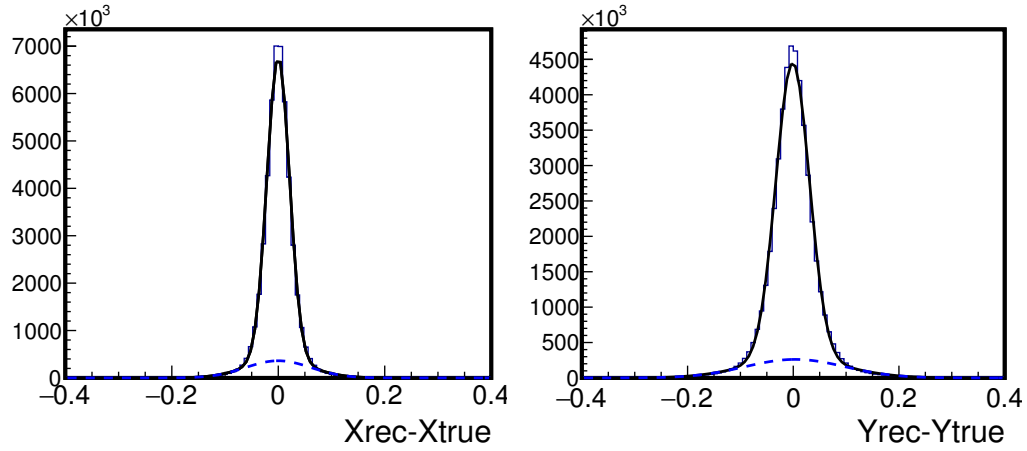

Figure 8. (Color online) Resolution of the Dalitz plot variables X (left) and Y (right) from the signal Monte Carlo simulations. The full line approximates the simulated distribution by a sum of two Gaussian functions; the dashed line represent the contribution of the broader Gaussian. The standard deviation of the narrower Gaussian is used in the discussion of the Dalitz plot bin width.

JHEP05(2016)019

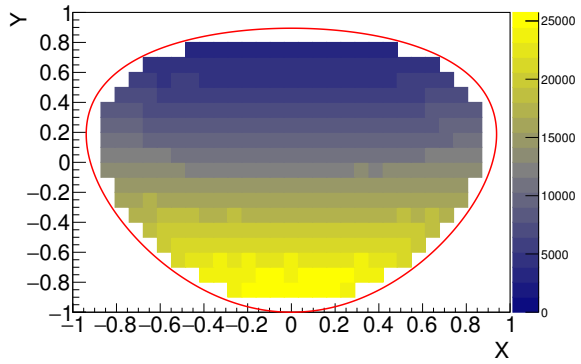

Figure 9. (Color online) The experimental background subtracted Dalitz plot distribution represented by the two dimensional histogram with 371 bins. Only bins used for the Dalitz parameter fits are shown. The physical border is indicated by the red line.

4 Dalitz plot

For the Dalitz plot, a two dimensional histogram representation is used. The bin width is determined both by the resolution in the X and Y variables and the number of events in each bin, which should be large enough to justify χ^2 fitting. The resolution of the X and Y variables is evaluated with MC signal simulation (figure 8). The distribution of the difference between the true and reconstructed values is fit with a sum of two Gaussian functions. The standard deviations of the narrower Gaussians are $\delta_X = 0.021$ and $\delta_Y = 0.032$. The range $(-1, 1)$ for the X and Y variables was divided into 31 and 20 bins, respectively. Therefore the bin widths correspond to approximately three standard deviations. The minimum bin content is $3.3 \cdot 10^3$ events. Figure 7 shows the distributions of the $\theta^*_{\gamma\gamma}$ and the $P^2_{\pi^0}$ variables for two bins in the Dalitz plot, one with the largest content and one with the smallest. As can be seen, the signal and the background are well reproduced by the simulation.

Figure 9 shows the experimental Dalitz plot distribution after background subtraction, which is fit to the amplitude expansion from eq. (1.5) to extract the Dalitz plot parameters. Only $n = 371$ bins which are fully inside the kinematic boundaries are used and there are $\sim 4.7 \cdot 10^6$ entries in the background subtracted Dalitz plot.

The fit is performed by minimizing the χ^2 like function

$$\chi^2 = \sum_{i=1}^{n} \left(\frac{N_i - \sum_{j=1}^{n_T} S_{ij} N_{T,j}}{\sigma_i} \right)^2 \tag{4.1}$$

where:

- $N_{T,j} = \int |A(X,Y)|^2 dPh(X,Y)_j$, with $|A(X,Y)|^2$ given by eq. (1.5). The integral is over X and Y in the allowed phase space for bin j. The sum over j bins includes all Dalitz plot bins at least partly inside the physical border, n_T.

- $N_i = N_{\mathrm{data},i} - \beta_1 B_{i1} - \beta_2 B_{i2}$ is the background subtracted content of Dalitz plot bin i, where $\beta_{1,2}$ are the scaling factors, B_{i1} is the $\omega\pi^0$ background in the bin i and B_{i2} is the same for the remaining background.

JHEP05(2016)019

Fit/set#	a	$b \cdot 10$	$d \cdot 10^2$	$f \cdot 10$	$g \cdot 10^2$	c, e, h, l	χ^2/dof	p-value
(1)	-1.095 ± 0.003	1.454 ± 0.030	8.11 ± 0.32	1.41 ± 0.07	-4.4 ± 0.9	free	354/361	0.60
(2)	-1.104 ± 0.002	1.533 ± 0.028	6.75 ± 0.27	0	0	0	1007/367	0
(3)	-1.104 ± 0.003	1.420 ± 0.029	7.26 ± 0.27	1.54 ± 0.06	0	0	385/366	0.24
(4)	-1.035 ± 0.002	1.598 ± 0.029	9.14 ± 0.33	0	-11.7 ± 0.9	free	792/362	0
(5)	-1.095 ± 0.003	1.454 ± 0.030	8.11 ± 0.33	1.41 ± 0.07	-4.4 ± 0.9	0	360/365	0.56
(6)	-1.092 ± 0.003	1.45 ± 0.03	8.1 ± 0.3	1.37 ± 0.06	-4.4 ± 0.9	0	369/365	0.43
(7)	-1.101 ± 0.003	1.41 ± 0.03	7.2 ± 0.3	1.50 ± 0.06	0	0	397/366	0.13

Table 2. Results for the Dalitz plot parameter fits. The main result corresponds to fit #5 which includes both cubic parameters g and f, while fit #3, with $g = 0$, can be directly compared to previous results. The fits #6 and #7 use the acceptance corrected data (see appendix A).

- S_{ij} is the acceptance and smearing matrix from bin j to bin i in the Dalitz plot. It is determined from signal MC by $S_{ij} = N_{\mathrm{rec},i;\mathrm{gen},j}/N_{\mathrm{gen},j}$, where $N_{\mathrm{rec},i;\mathrm{gen},j}$ denotes the number of events reconstructed in bin i which were generated in bin j and $N_{\mathrm{gen},j}$ denotes the total number of events generated in bin j.

- $\sigma_i^2 = \sigma_{N_i}^2 + \sigma_{S_{ij}}^2$ is the error in bin i, with $\sigma_{S_{ij}}^2 = \sum_{j=1}^{n_T} N_{T,j}^2 \cdot S_{ij} \cdot (1 - S_{ij})/N_{\mathrm{gen},j}$.

The input-output test of the fit procedure was performed using signal MC generated with the same statistics as the experimental data. The extracted values for the parameters were within one standard deviation with respect to the input.

The fit has been performed using different choices of the free parameters in eq. (1.5), with the normalization N and the parameters a, b and d always let free. The main fit results are summarized in table 2. The first row (set #1) includes all parameters of the cubic expansion, eq. (1.5). The fit values of the charge conjugation violating parameters c, e, h and l are consistent with zero ($c = (4.3 \pm 3.4) \cdot 10^{-3}$, $e = (2.5 \pm 3.2) \cdot 10^{-3}$, $h = (1.1 \pm 0.9) \cdot 10^{-2}$, $l = (1.1 \pm 6.5) \cdot 10^{-3}$) and are omitted from the table. Therefore our main results are obtained with the charge conjugation violating parameters c, e, h and l set to zero. Fit #2 with $f = g = 0$ demonstrates that it is not possible to describe the experimental distribution with only quadratic terms. Fit #3 including the f parameter and with $g = 0$ gives a reasonable χ^2/ndf value of 385/366. On the contrary the complementary selection of the cubic parameters $f = 0$ and g free (fit #4) does not provide adequate description of the data. Finally fit #5 which includes both f and g parameters, gives the g parameter negative and different from zero at the 4.9σ level. To compare goodness of the fit between cases #3 and #5 one should remember that the parameters in the two fits are the same except for one extra parameter in fit #5. Therefore if the g parameter is not significant we expect that the $\chi^2_{set\#3} - \chi^2_{set\#5}$ variable will have chi squared distribution with one degree of freedom. The determined value of 25 allows us to prefer fit #5 over #3. In case of uncorrelated parameters one expects the chi square difference has a non-central chi squared distribution with one degree of freedom and the mean value of $(g/\sigma_g)^2$ fully consistent with the data. However, in the further discussions we include also set #3 with

JHEP05(2016)019

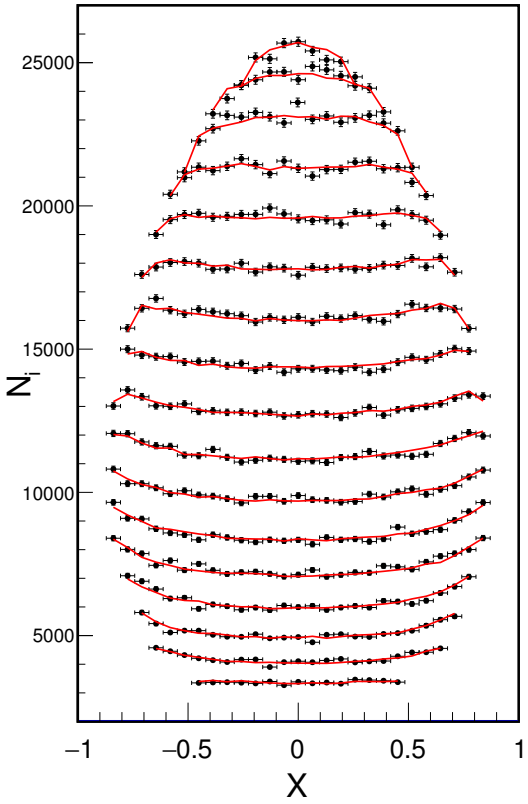

Figure 10. (Color online) The experimental background subtracted Dalitz plot data, N_i, (points with errors), compared to set #5 fit results (red lines connecting bins with the same Y value). The row with lowest N_i values corresponds to the highest Y value ($Y = +0.75$).

$g = 0$, since it enables a more direct comparison to the previous experiments (KLOE(08), WASA(14) and BESIII(15)). The correlation matrices for fits #3 and #5 are:

	b	d	f
a	-0.269	-0.365	-0.832
b		$+0.333$	-0.139
d			$+0.089$

	b	d	f	g
a	-0.120	$+0.044$	-0.859	-0.534
b		$+0.389$	-0.201	-0.225
d			-0.160	-0.557
f				$+0.408.$

The fit #5 is compared to the background subtracted Dalitz plot data, N_i, in figure 10. The red lines represent the fit result and correspond to separate slices in the Y variable. Figure 11 shows the distribution of the normalized residuals for the fit #5: $r_i = (N_i -$

JHEP05(2016)019

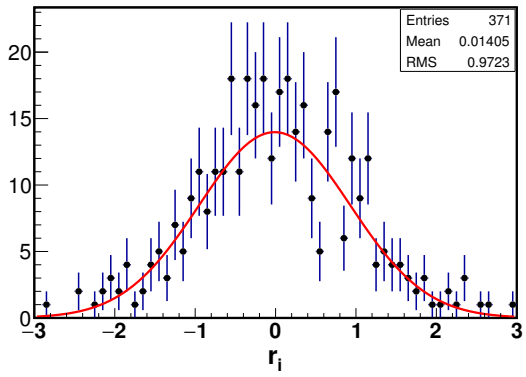

Figure 11. (Color online) Distribution of the normalized residuals, r_i, for fit #5.

Experiment	$A_{LR} \times 10^{-2}$	$A_Q \times 10^{-2}$	$A_S \times 10^{-2}$
Gormley(68) [27]	$+1.5 \pm 0.5$	–	0.5 ± 0.5
Layter(72) [28]	-0.05 ± 0.22	-0.07 ± 0.22	0.10 ± 0.22
Jane(74) [29]	$+0.28 \pm 0.26$	-0.30 ± 0.25	0.20 ± 0.25
KLOE(08) [19]	$+0.09 \pm 0.10^{+0.09}_{-0.14}$	$-0.05 \pm 0.010^{+0.03}_{-0.05}$	$0.08 \pm 0.10^{+0.08}_{-0.13}$
KLOE(this work)	$-0.050 \pm 0.045^{+0.050}_{-0.11}$	$0.020 \pm 0.045^{+0.048}_{-0.023}$	$0.004 \pm 0.045^{+0.033}_{-0.035}$

Table 3. Results on the asymmetry parameters.

$\sum_{j=1}^{n} S_{ij} N_{T,j})/\sigma_i$. The location of the residuals $r_i > 1$ and $r_i < -1$ on the Dalitz plot is uniform. The fits #6 and #7 use the acceptance corrected data (see appendix A).

5 Asymmetries

While the extracted Dalitz plot parameters are consistent with charge conjugation symmetry, the unbinned integrated charge asymmetries provide a more sensitive test. The left-right (A_{LR}), quadrant (A_Q) and sextant (A_S) asymmetries are defined in ref. [28]. The same background subtraction is applied as for the Dalitz plot parameter analysis. For each region in the Dalitz plot used in the calculation of the asymmetries, the acceptance is calculated from the signal MC as the ratio between the number of the reconstructed and the generated events. The yields are then corrected for the corresponding efficiency. The procedure was tested using signal MC generated with the same statistics as the experimental data. The results for the asymmetries are presented in the table 3 and compared to other experiments. The statistical accuracy for all asymmetries in the present analysis is $4.5 \cdot 10^{-4}$. The discussion of the systematical uncertainties is given in section 6.

6 Systematic checks

To quantify and account for systematic effects in the results, several checks have been made.

JHEP05(2016)019

- Minimum photon energy cut (EGmin) is changed from 10 MeV to 20 MeV (for comparison the EMC energy resolution varies from 60% to 40% for this energy range). The systematic error is taken as half of the difference.

- Background subtraction (BkgSub) is checked by determining the background scaling factors for each bin (or region for the asymmetries) of the Dalitz plot separately. With the same method as for the whole data sample, using the $\theta^*_{\gamma\gamma}$ and $P^2_{\pi^0}$ distributions, background scaling factors are determined for each bin (or region). The systematic error is taken as half the difference with the standard result.

- Choice of binning (BIN) is tested by varying number of bins of the Dalitz plot. For X and Y simultaneously, the bin width is varied from $\sim 2\delta_{X,Y}$ to $\sim 5\delta_{X,Y}$, in total 10 configurations. The systematic uncertainty is given by the standard deviation of the results.

- $\theta_{+\gamma}, \theta_{-\gamma}$ cut: the areas of the three zones shown in figure 1 were simultaneously varied by $\pm 10\%$.

- $\Delta t_e, \Delta t_\pi$ cut: the offsets of the horizontal and diagonal lines shown in figure 2 were varied by ± 0.22 ns and ± 0.21 ns, respectively.

- $\theta^*_{\gamma\gamma}$ cut is varied by $\pm 3^\circ$, corresponding to $\sim 1\sigma$.

- Missing mass cut (MM) is tested by varying the cut by ± 2.0 MeV, $\sim 1\sigma$. For this cut a stronger dependence of the parameters on the cut was noted. This has been further investigated by performing the Dalitz plot parameter fit for one parameter at a time, for each step, and keeping the other parameters fixed at the value for the standard result. Since the dependence was reduced when varying just one parameter, we conclude that it is mostly due to the correlations between parameters.

- Event classification procedure (ECL) is investigated by using a prescaled data sample without the event classification bias (collected with prescaling factor 1/20). The fraction of events remaining in each Dalitz plot bin after the event classification conditions varies between 94% and 80% for different bins and it is very well described by the MC within the errors. The analysis of the prescaled data follows the standard chain. The systematic error is extracted as half the difference between the results of the analysis with and without the event classification procedure.

Unless stated otherwise the systematic error is calculated as the difference between the two tests and the standard result. If both differences have the same sign, the asymmetric error is taken with one boundary set at zero and the other at the largest of the differences. The resulting systematic error contributions for the Dalitz plot parameters for the sets #5 and #3 are summarized in table 4 and table 5, respectively. The systematic error contributions for the charge asymmetries are summarized in table 6.

JHEP05(2016)019

syst. error ($\times 10^4$)	Δa	Δb	Δd	Δf	Δg
EGmin	± 6	± 12	± 10	± 5	± 16
BkgSub	± 8	± 7	± 11	± 6	± 38
BIN	± 17	± 13	± 9	± 36	± 44
$\theta_{+\gamma}, \theta_{-\gamma}$ cut	$^{+0}_{-1}$	$^{+0}_{-2}$	$^{+2}_{-2}$	$^{+3}_{-0}$	$^{+3}_{-2}$
Δt_e cut	$^{+\ 6}_{-11}$	$^{+12}_{-\ 1}$	$^{+18}_{-\ 1}$	$^{+3}_{-8}$	$^{+26}_{-54}$
$\Delta t_e - \Delta t_\pi$ cut	± 0	$^{+0}_{-1}$	$^{+3}_{-1}$	± 0	$^{+2}_{-1}$
$\theta^*_{\gamma\gamma}$ cut	$^{+14}_{-\ 5}$	$^{+2}_{-1}$	$^{+21}_{-12}$	$^{+\ 5}_{-25}$	$^{+26}_{-38}$
MM	$^{+\ 8}_{-10}$	$^{+46}_{-43}$	$^{+49}_{-45}$	$^{+57}_{-62}$	$^{+100}_{-\ 92}$
ECL	± 0	± 8	± 6	± 9	± 12
TOTAL	$^{+26}_{-25}$	$^{+52}_{-48}$	$^{+59}_{-50}$	$^{+69}_{-77}$	$^{+123}_{-129}$

Table 4. Summary of the systematic errors for a, b, d, f, g parameters (fit #5).

syst. error ($\times 10^4$)	Δa	Δb	Δd	Δf
EGmin	± 9	± 10	± 6	± 0
BkgSub	± 1	± 5	± 6	± 8
BIN	± 9	± 14	± 9	± 26
$\theta_{+\gamma}, \theta_{-\gamma}$ cut	$^{+0}_{-1}$	$^{+0}_{-2}$	$^{+1}_{-1}$	$^{+4}_{-0}$
Δt_e cut	$^{+0}_{-6}$	$^{+14}_{-\ 6}$	$^{+7}_{-0}$	$^{+19}_{-15}$
$\Delta t_e - \Delta t_\pi$ cut	± 0	$^{+0}_{-1}$	$^{+3}_{-0}$	± 0
$\theta^*_{\gamma\gamma}$ cut	$^{+6}_{-0}$	$^{+1}_{-1}$	$^{+14}_{-\ 8}$	$^{+\ 0}_{-13}$
MM	$^{+10}_{-10}$	$^{+39}_{-36}$	$^{+31}_{-26}$	$^{+28}_{-35}$
ECL	± 2	± 9	± 9	± 13
TOTAL	$^{+18}_{-18}$	$^{+46}_{-41}$	$^{+38}_{-31}$	$^{+45}_{-51}$

Table 5. Summary of the systematic errors for a, b, d, f parameters (fit #3).

7 Discussion

The final results for the Dalitz plot parameters, including systematic effects, are therefore:

$$a = -1.095 \pm 0.003^{+0.003}_{-0.002}$$
$$b = +0.145 \pm 0.003 \pm 0.005$$
$$d = +0.081 \pm 0.003^{+0.006}_{-0.005}$$
$$f = +0.141 \pm 0.007^{+0.007}_{-0.008}$$
$$g = -0.044 \pm 0.009^{+0.012}_{-0.013}$$

JHEP05(2016)019

syst. error ($\times 10^5$)	ΔA_{LR}	ΔA_Q	ΔA_S
EGmin	± 1	± 0	± 4
BkgSub	± 5	± 3	± 16
$\theta_{+\gamma}, \theta_{-\gamma}$ cut	$^{+2}_{-0}$	$^{+0}_{-2}$	$^{+2}_{-0}$
Δt_e cut	$^{+49}_{-92}$	$^{+48}_{-22}$	$^{+\ 7}_{-15}$
$\Delta t_e - \Delta t_\pi$ cut	$^{+0}_{-2}$	$^{+3}_{-0}$	$^{+0}_{-1}$
$\theta^*_{\gamma\gamma}$ cut	$^{+\ 1}_{-57}$	$^{+3}_{-4}$	$^{+0}_{-8}$
MM	$^{+0}_{-4}$	$^{+0}_{-1}$	$^{+1}_{-2}$
ECL	± 9	± 0	± 25
TOTAL	$^{+\ 50}_{-109}$	$^{+48}_{-23}$	$^{+31}_{-35}$

Table 6. Summary of the systematic errors for the asymmetries.

including the g parameter. With g parameter set to zero the results are:

$$\begin{aligned} a &= -1.104 \pm 0.003 \pm 0.002 \\ b &= +0.142 \pm 0.003^{+0.005}_{-0.004} \\ d &= +0.073 \pm 0.003^{+0.004}_{-0.003} \\ f &= +0.154 \pm 0.006^{+0.004}_{-0.005}. \end{aligned}$$

These results confirm the tension with the theoretical calculations on the b parameter, and also the need for the f parameter. In comparison to the previous measurements shown in table 1, the present results are the most precise and the first including the g parameter. The improvement over KLOE(08) analysis comes from four times larger statistics and improvement in the systematic uncertainties which are in some cases reduced by factor $2-3$. The major improvement in the systematic uncertainties comes from the analysis of the effect of the Event classification with an unbiased prescaled data sample.

The final values of the charge asymmetries are all consistent with zero:

$$\begin{aligned} A_{LR} &= (-5.0 \pm 4.5^{+5.0}_{-11}) \cdot 10^{-4} \\ A_Q &= (+1.8 \pm 4.5^{+4.8}_{-2.3}) \cdot 10^{-4} \\ A_S &= (-0.4 \pm 4.5^{+3.1}_{-3.5}) \cdot 10^{-4}. \end{aligned}$$

The systematic and statistical uncertainties are of the same size except for the A_{LR} which is dominated by the systematic uncertainty due to the description of the Bhabha background.

JHEP05(2016)019

Acknowledgments

We warmly thank our former KLOE colleagues for the access to the data collected during the KLOE data taking campaign. We thank the DAΦNE team for their efforts in maintaining low background running conditions and their collaboration during all data taking. We want to thank our technical staff: G.F. Fortugno and F. Sborzacchi for their dedication in ensuring efficient operation of the KLOE computing facilities; M. Anelli for his continuous attention to the gas system and detector safety; A. Balla, M. Gatta, G. Corradi and G. Papalino for electronics maintenance; M. Santoni, G. Paoluzzi and R. Rosellini for general detector support; C. Piscitelli for his help during major maintenance periods. This work was supported in part by the EU Integrated Infrastructure Initiative Hadron Physics Project under contract number RII3-CT- 2004-506078; by the European Commission under the 7th Framework Programme through the 'Research Infrastructures' action of the 'Capacities' Programme, Call: FP7-INFRASTRUCTURES-2008-1, Grant Agreement No. 227431; by the Polish National Science Centre through the Grants No. 2011/03/N/ST2/02652, 2013/08/M/ST2/00323, 2013/11/B/ST2/04245, 2014/14/E/ST2/00262, 2014/12/S/ST2/00459.

A Acceptance corrected data

With a smearing matrix close to diagonal and the smearing to and from nearby bins symmetrical, the acceptance corrected data can be used instead of dealing with the smearing matrix. This representation has the advantage of being much easier to compare directly with theoretical calculations. The acceptance corrected signal content in each bin of the Dalitz plot is obtained by dividing the background subtracted content, N_i, by the corresponding acceptance, ϵ_i. The acceptance is obtained from the signal MC by dividing the number of reconstructed events allocated to the bin i by the number of generated (unsmeared) signal events in that bin.

The fit to extract the Dalitz plot parameters values is done now by minimizing

$$\chi^2 = \sum_{i=1}^{n} \left(\frac{N_i/\epsilon_i - N_{T,i}}{\sigma_i} \right)^2 \tag{A.1}$$

where the sum includes only bins completely inside the Dalitz plot boundaries and $N_{T,i} = \int\int |A(X,Y)|^2 dX_i dY_i$. The statistical uncertainty σ_i includes contributions from the experimental data, the background estimated from MC and the efficiency. The fitted Dalitz plot parameters using the acceptance corrected data are presented in table 2 as sets #6 with g parameter and #7 with $g = 0$. The results are identical within statistical uncertainties with the values obtained using the smearing matrix. Therefore the acceptance corrected data can be used to represent the measured Dalitz plot density if one neglects systematical uncertainties. The table containing Dalitz plot acceptance corrected data (normalized to the content of the $X_c = 0.0, Y_c = 0.05$ bin), is provided as a supplementary material (file `DPhist_acccorr.txt`). The correlation matrix for the fit #6 reads:

JHEP05(2016)019

	b	d	f	g
a	-0.110	$+0.006$	-0.849	-0.512
b		$+0.397$	-0.216	-0.239
d			-0.133	-0.537
f				$+0.380.$

References

[1] D.G. Sutherland, *Current algebra and the decay* $\eta \to 3\pi$, *Phys. Lett.* **23** (1966) 384 [INSPIRE].

[2] J.S. Bell and D.G. Sutherland, *Current algebra and* $\eta \to 3\pi$, *Nucl. Phys.* **B 4** (1968) 315 [INSPIRE].

[3] R. Baur, J. Kambor and D. Wyler, *Electromagnetic corrections to the decays* $\eta \to 3\pi$, *Nucl. Phys.* **B 460** (1996) 127 [hep-ph/9510396] [INSPIRE].

[4] C. Ditsche, B. Kubis and U.-G. Meißner, *Electromagnetic corrections in* $\eta \to 3\pi$ *decays*, *Eur. Phys. J.* **C 60** (2009) 83 [arXiv:0812.0344] [INSPIRE].

[5] J. Bijnens and J. Gasser, *Eta decays at and beyond* p^4 *in chiral perturbation theory*, *Phys. Scripta* **T 99** (2002) 34 [hep-ph/0202242] [INSPIRE].

[6] H. Leutwyler, *The ratios of the light quark masses*, *Phys. Lett.* **B 378** (1996) 313 [hep-ph/9602366] [INSPIRE].

[7] R.F. Dashen, *Chiral* SU(3) × SU(3) *as a symmetry of the strong interactions*, *Phys. Rev.* **183** (1969) 1245 [INSPIRE].

[8] J. Gasser and H. Leutwyler, $\eta \to 3\pi$ *to one loop*, *Nucl. Phys.* **B 250** (1985) 539 [INSPIRE].

[9] Particle Data Group collaboration, K.A. Olive et al., *Review of particle physics*, *Chin. Phys.* **C 38** (2014) 090001 [INSPIRE].

[10] J. Bijnens and K. Ghorbani, $\eta \to 3\pi$ *at two loops in chiral perturbation theory*, *JHEP* **11** (2007) 030 [arXiv:0709.0230] [INSPIRE].

[11] B. Borasoy and R. Nissler, *Hadronic* η *and* η' *decays*, *Eur. Phys. J.* **A 26** (2005) 383 [hep-ph/0510384] [INSPIRE].

[12] S.P. Schneider, B. Kubis and C. Ditsche, *Rescattering effects in* $\eta \to 3\pi$ *decays*, *JHEP* **02** (2011) 028 [arXiv:1010.3946] [INSPIRE].

[13] K. Kampf, M. Knecht, J. Novotný and M. Zdráhal, *Analytical dispersive construction of* $\eta \to 3\pi$ *amplitude: first order in isospin breaking*, *Phys. Rev.* **D 84** (2011) 114015 [arXiv:1103.0982] [INSPIRE].

[14] G. Colangelo, S. Lanz, H. Leutwyler and E. Passemar, *Determination of the light quark masses from* $\eta \to 3\pi$, PoS(EPS-HEP2011)304 [INSPIRE].

[15] P. Guo et al., *Three-body final state interaction in* $\eta \to 3\pi$, *Phys. Rev.* **D 92** (2015) 054016 [arXiv:1505.01715] [INSPIRE].

JHEP05(2016)019

[16] M. Gormley et al., *Experimental determination of the Dalitz-plot distribution of the decays $\eta \to \pi^+\pi^-\pi^0$ and $\eta \to \pi^+\pi^-\gamma$ and the branching ratio $\eta \to \pi^+\pi^-\gamma/\eta \to \pi^+$*, *Phys. Rev.* **D 2** (1970) 501 [INSPIRE].

[17] J.G. Layter et al., *Study of Dalitz-plot distributions of the decays $\eta \to \pi^+\pi^-\pi^0$ and $\eta \to \pi^+\pi^-\gamma$*, *Phys. Rev.* **D 7** (1973) 2565 [INSPIRE].

[18] CRYSTAL BARREL collaboration, A. Abele et al., *Momentum dependence of the decay $\eta \to \pi^+\pi^-\pi^0$*, *Phys. Lett.* **B 417** (1998) 197 [INSPIRE].

[19] KLOE collaboration, F. Ambrosino et al., *Determination of $\eta \to \pi^+\pi^-\pi^0$ Dalitz plot slopes and asymmetries with the KLOE detector*, *JHEP* **05** (2008) 006 [arXiv:0801.2642] [INSPIRE].

[20] WASA-AT-COSY collaboration, P. Adlarson et al., *Measurement of the $\eta \to \pi^+\pi^-\pi^0$ Dalitz plot distribution*, *Phys. Rev.* **C 90** (2014) 045207 [arXiv:1406.2505] [INSPIRE].

[21] BESIII collaboration, M. Ablikim et al., *Measurement of the matrix elements for the decays $\eta \to \pi^+\pi^-\pi^0$ and $\eta/\eta' \to \pi^0\pi^0\pi^0$*, *Phys. Rev.* **D 92** (2015) 012014 [arXiv:1506.05360] [INSPIRE].

[22] J. Kambor, C. Wiesendanger and D. Wyler, *Final state interactions and Khuri-Treimanequations in $\eta \to 3\pi$ decays*, *Nucl. Phys.* **B 465** (1996) 215 [hep-ph/9509374] [INSPIRE].

[23] M. Adinolfi et al., *The tracking detector of the KLOE experiment*, *Nucl. Instrum. Meth.* **A 488** (2002) 51 [INSPIRE].

[24] M. Adinolfi et al., *The KLOE electromagnetic calorimeter*, *Nucl. Instrum. Meth.* **A 482** (2002) 364 [INSPIRE].

[25] KLOE collaboration, M. Adinolfi et al., *The trigger system of the KLOE experiment*, *Nucl. Instrum. Meth.* **A 492** (2002) 134 [INSPIRE].

[26] F. Ambrosino et al., *Data handling, reconstruction and simulation for the KLOE experiment*, *Nucl. Instrum. Meth.* **A 534** (2004) 403 [physics/0404100] [INSPIRE].

[27] M. Gormley et al., *Experimental test of C invariance in $\eta \to \pi^+\pi^-\pi^0$*, *Phys. Rev. Lett.* **21** (1968) 402 [INSPIRE].

[28] J.G. Layter et al., *Measurement of the charge asymmetry in the decay $\eta \to \pi^+\pi^-\pi^0$*, *Phys. Rev. Lett.* **29** (1972) 316 [INSPIRE].

[29] M.R. Jane et al., *A measurement of the charge asymmetry in the decay $\eta \to \pi^+\pi^-\pi^0$*, *Phys. Lett.* **B 48** (1974) 260 [INSPIRE].

JHEP05(2016)019